Probing quantum critical dynamics on a programmable Rydberg simulator

Alexander Keesling,[1] Ahmed Omran,[1] Harry Levine,[1] Hannes Bernien,[1] Hannes Pichler,[1,2] Soonwon Choi,[1] Rhine Samajdar,[1] Sylvain Schwartz,[3] Pietro Silvi,[4] Subir Sachdev,[1] Peter Zoller,[4] Manuel Endres,[5] Markus Greiner,[1] Vladan Vuletić,[6] and Mikhail D. Lukin[1]

[1]*Department of Physics, Harvard University, Cambridge, MA 02138, USA*
[2]*ITAMP, Harvard-Smithsonian Center for Astrophysics, Cambridge, MA 02138, USA*
[3]*Laboratoire Kastler Brossel, ENS-PSL Research University, CNRS, UPMC-Sorbonne Universités, Collège de France, 24 rue Lhomond, 75005 Paris, France*
[4]*Institute for Quantum Optics and Quantum Information, Austrian Academy of Sciences & Center for Quantum Physics, University of Innsbruck, Innsbruck A-6020, Austria*
[5]*Division of Physics, Mathematics and Astronomy, California Institute of Technology, Pasadena, CA 91125, USA*
[6]*Department of Physics and Research Laboratory of Electronics, Massachusetts Institute of Technology, Cambridge, MA 02139, USA*

Quantum phase transitions (QPTs) involve transformations between different states of matter that are driven by quantum fluctuations [1]. These fluctuations play a dominant role in the quantum critical region surrounding the transition point, where the dynamics are governed by the universal properties associated with the QPT. The resulting quantum criticality has been explored by probing linear response for systems near thermal equilibrium [2, 3]. While time-dependent phenomena associated with classical phase transitions have been studied in various scientific fields [4–8], understanding critical real-time dynamics in isolated, non-equilibrium quantum systems is of fundamental importance both for exploring novel approaches to quantum information processing [9] and realizing exotic new phases of matter [10]. Here, we use a Rydberg atom quantum simulator with programmable interactions to study the quantum critical dynamics associated with several distinct QPTs. By studying the growth of spatial correlations while crossing the QPT at variable speeds, we experimentally verify the quantum Kibble-Zurek mechanism (QKZM) [11–13] for an Ising-type QPT, explore scaling universality, and observe corrections beyond simple QKZM predictions. This approach is subsequently used to investigate novel QPTs associated with chiral clock models [14, 15], providing new insights into exotic systems, and opening the door for precision studies of critical phenomena and applications to quantum optimization.

The celebrated Kibble-Zurek hypothesis [4, 5] describes nonequilibrium dynamics and the formation of topological defects in a second-order phase transition resulting from changes in temperature or pressure [6–8]. Recently, the concepts underlying the Kibble-Zurek description have been extended to the quantum regime [11–13]. Here, the typical size of the correlated regions, ξ, after a dynamical sweep across the QPT scales as a power-law of the sweep rate, v, with an exponent, μ, determined entirely by the QPT's universality class. Specifically, QKZM postulates that when the time scale over which the Hamiltonian changes becomes faster than the characteristic response time, τ_h, determined by the inverse of the energy gap between the ground and excited states, nonadiabatic excitations prevent the continued growth of correlated regions (Fig. 1a). The resulting scaling exponent, $\mu = \nu/(1+\nu z)$, is determined by a combination of the critical exponent ν, that characterizes the divergent correlation length, and the dynamical critical exponent z, that characterizes the relative scaling of space and time close to the critical point [1]. Such non-equilibrium quantum critical dynamics is challenging to observe, in particular due to coupling of many-body systems to the environment as evidenced by experiments in superconducting systems [16, 17]. Recently, experimental control over isolated quantum systems enabled the observation of scaling behavior across phase transitions described by mean-field theories [18, 19]. While important aspects of QPTs have already been explored in strongly correlated systems [20], experimental probing of quantum critical phenomena beyond mean-field in real-time dynamics remains an outstanding challenge [21, 22].

We probe quantum criticality using a reconfigurable 1D array of ^{87}Rb atoms with programmable interactions [23] (Supplementary Information). In our system, atoms in the electronic ground state $|g\rangle$, evenly separated by a controllable distance, are homogeneously coupled to the excited Rydberg state $|r\rangle$, in which they experience van der Waals interactions with a strength that decays as $V(r) \propto 1/r^6$, where r is the interatomic distance. This system is described by the many-body Hamiltonian,

$$\frac{\mathcal{H}}{\hbar} = \frac{\Omega}{2}\sum_i \sigma_i^x - \Delta \sum_i n_i + \sum_{i<j} V_{ij} n_i n_j, \qquad (1)$$

where $n_i = |r_i\rangle\langle r_i|$ is the projector onto the Rydberg state at site i, $\sigma_i^x = |g_i\rangle\langle r_i| + |r_i\rangle\langle g_i|$, Δ and Ω are the detuning and Rabi frequency of the coherent laser coupling between $|g\rangle$ and $|r\rangle$, and V_{ij} is the interaction strength between atoms in the Rydberg state at sites i and j. For negative values of Δ, the many-body ground state corresponds to a disordered phase, in which all atoms are in the electronic ground state $|g\rangle$. For $\Delta > 0$, several spa-

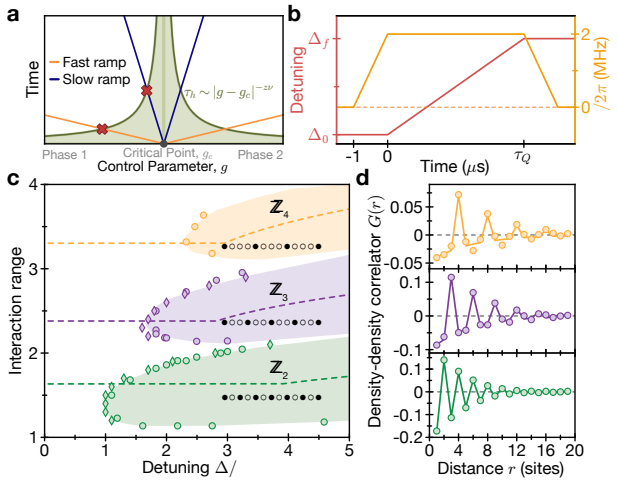

FIG. 1: **Quantum Kibble-Zurek mechanism and phase diagram.** **a**, Illustration of the QKZM. As the control parameter approaches its critical value, the response time, given by the inverse energy gap of the system, diverges. When the temporal distance to the critical point becomes equal to the response time, τ_h, as marked by red crosses, the correlations stop growing. **b**, Sequence diagram used for measurements. **c**, Numerically calculated ground-state phase diagram. Circles (diamonds) denote numerically obtained points along the phase boundaries calculated using (infinite-size) Density-Matrix Renormalization Group techniques (see Supplementary Information). The shaded regions are a guide to the eye, and do not correspond to numerical calculations of the phase boundaries. Dashed lines show the experimental trajectories across the phase transitions. **d**, Measured (circles) density-density Rydberg correlations with fits to the expected ordered pattern (solid lines) consistent with $\mathbb{Z}_4$- (orange), $\mathbb{Z}_3$- (purple) and $\mathbb{Z}_2$-ordered (green) states. Error bars denote the standard error of the mean (s.e.m.) and are smaller than the marker size.

tially ordered phases arise from the competition between the detuning term, which favors a large Rydberg fraction, and the Rydberg blockade [24], which prohibits simultaneous excitation of atoms separated by a distance smaller than the blockade radius, R_B, defined via $V(R_B) \equiv \Omega$. As illustrated in Fig. 1c,d, we probe different QPTs into states breaking various symmetries by choosing the interatomic spacing, and sweeping the control parameter, Δ, across the phase boundary. These QPTs belong to different universality classes, including instances that are not yet fully understood theoretically, and which have eluded experimental investigations.

We first focus on the QPT from the disordered phase into the antiferromagnetic phase with broken $\mathbb{Z}_2$ symmetry, which is known to belong to the Ising universality class [1]. Using an interatomic spacing, a, such that $R_B/a \sim 1.69$, we create an array of 51 atoms in the electronic ground state, and slowly turn on Ω at $\Delta < 0$, adiabatically preparing the system in the ground state of the disordered phase. The detuning is then increased over a quenching time τ_Q at a constant rate, v, up to a final value Δ_f, at which point Ω is slowly turned off (see Fig. 1b), and the state of every atom is measured. We examine the dynamical development of correlations between the atoms, characterized by the Rydberg density-density correlation function:

$$G(r) = \sum_i (\langle n_i n_{i+r} \rangle - \langle n_i \rangle \langle n_{i+r} \rangle)/N_r, \qquad (2)$$

where the normalization N_r is the number of pairs of sites separated by distance r. By fitting an exponential decay to the modulus of the correlation function, we extract the correlation length (see Supplementary Information). The experimental results show growth of the correlation length as the detuning approaches the critical point, followed by saturation once the detuning is swept past the critical point into the ordered phase (Fig. 2b). From the individual images, it is apparent that, while for fast sweeps the ordered domains are frequently interrupted by defects (domain walls), for slow ramps, significantly longer domains are observed (Fig. 2a). A systematic analysis of the final correlation lengths after crossing into the ordered phase shows that a power-law scaling model $\xi(v) = \xi_0(v_0/v)^\mu$ with $\mu = 0.50(3)$ accurately describes our measurements (Fig. 2c) (Supplementary Information). These results are consistent with numerical simulations (red points) of the coherent evolution of the system using Matrix Product States (MPS).

The QPT into the $\mathbb{Z}_2$-ordered phase is in the Ising universality class [1], with critical exponents in 1D of $z = 1$, $\nu = 1$, and consequently, $\mu_{\rm ISING} = 0.5$. Our observations are consistent with these quantitative predictions, and are quite distinct from those associated with a mean-field Ising transition, described by $z = 1$, $\nu = 1/2$, and yielding $\mu_{\rm MF} = 1/3$ [18, 25].

A key concept associated with critical phenomena is that of universality, which is manifested by the collapse of correlations to a universal form when rescaled according to the corresponding critical exponents. Such a signature is a strong test of an underlying universal scaling law, and in connection with the QKZM, should appear upon rescaling lengths by $(v/v_0)^\mu$. Fig. 3a shows that the rescaled correlations for $R_B/a \sim 1.81$ indeed collapse onto two smooth branches, which in turn collapse on top of each other when the correlations are rectified as $(-1)^r G(r)$ (inset in Fig. 3a), according to the $\mathbb{Z}_2$ order parameter. While the Kibble-Zurek hypothesis is a coarse-grained theory predicting the mean density of defects, the shape of the correlation function gives further access to microscopic details of the system. Detailed inspection of the rescaled correlation functions reveals nontrivial deviations from a simple exponential decay. In particular, the correlations in Fig. 3a become negative for a range of distances, which implies complex dynamics in the formation and spreading of defects. The observed

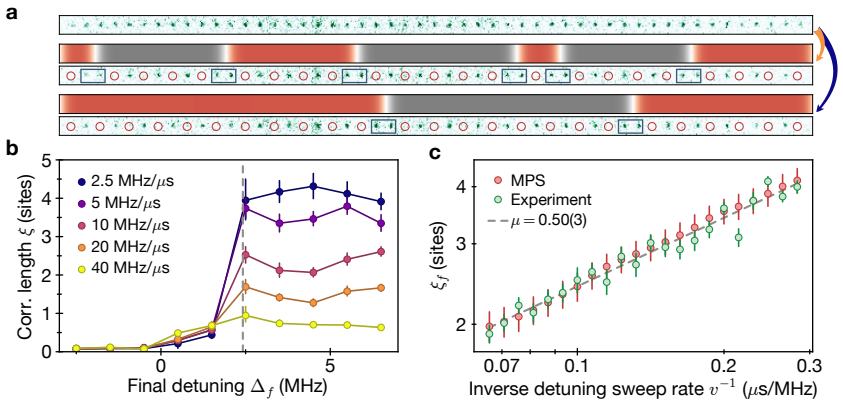

FIG. 2: **QKZM for QPT into a $\mathbb{Z}_2$-ordered phase. a**, Single-shot images of the atom array before and after a fast and a slow sweep across the phase transition, showing larger average sizes of correlated domains for the slower sweep. Green spots (open circles) represent atoms in $|g\rangle$ ($|r\rangle$). Blue rectangles mark the position of domain walls, and the colored areas above show the different ordered regions. **b**, Correlation length growth and saturation as the system crosses the QPT at different rates. The gray dashed line indicates the critical detuning. **c**, Dependence of correlation length on inverse sweep rate across the phase transition with experimentally measured (green) and MPS-simulated results (red). The length is extracted from fitting the modulus of the correlation data to an exponential decay. Error bars denote fit uncertainty. The dashed line indicates a power-law fit with a scaling exponent $\mu = 0.50(3)$ for the experiment.

corrections to simple QKZM predictions are consistent with previous theoretical analyses [26, 27] and are in good agreement with theoretical simulations using MPS (Fig. 3c). Finally, applying the universal rescaling to the correlation growth shown in Fig. 2b allows us to independently estimate the values of critical exponents (Supplementary Information, Fig. S7), showing that our results are consistent with $z = \nu = 1$ associated with the Ising QPT.

Having established the validity of the QKZM, as well as its limitations, for a QPT in the Ising universality class, we now explore transitions into more complex $\mathbb{Z}_N$-ordered phases, where Rydberg excitations are evenly separated by $N > 2$ sites (see Fig. 1c). The correlation functions at smaller interatomic spacings after slow detuning sweeps reflect the spatial ordering of the $\mathbb{Z}_3$- and $\mathbb{Z}_4$-ordered phases (Fig. 1d). In addition, we determine the probability of finding two Rydberg excitations separated by N-sites, for each value of N and R_B (Fig. 4b) (Supplementary Information). Combining these measurements with the numerically obtained critical points (see Fig. 1c), we experimentally identify approximate boundaries for the regions consistent with the $\mathbb{Z}_2$-, $\mathbb{Z}_3$-, and $\mathbb{Z}_4$-ordered phases in Fig. 4b. Within these regions, the dominant type of order is the one associated with the corresponding phase, while the second most prevalent type of order arises from the lowest-energy (most probable) defects. In particular, we observe that in the $\mathbb{Z}_3$-ordered phase, the most-likely defect changes from $\mathbb{Z}_2$-like for smaller values of R_B, to $\mathbb{Z}_4$-like as R_B increases.

We test for a power-law scaling behavior of the correlation length growth as a function of ramp speed at different interaction strengths in Fig. 4c. To consistently compare the results for all interaction strengths, we fit the correlation function to an exponentially decaying density wave with a period set by the underlying order (as opposed to the modulus of the correlation function used in Fig. 2c, see Supplementary Information). The scaling is extracted through a power-law fit to the resulting correlation lengths. In parameter regimes far away from regions of competing order, we observe three stable plateaus for the regions consistent with $\mathbb{Z}_2$, $\mathbb{Z}_3$, and $\mathbb{Z}_4$ order, respectively. For interaction strengths where there is a strong competition between different types of order, we do not observe the formation of long-range correlations (pale points in Fig. 4c). In these cases, the detuning sweeps either do not fully cross the phase boundary into the ordered phases (Supplementary Information) or potentially enter theoretically predicted incommensurate phases [15, 29].

To understand our observations, we compare them to finite-size scaling analyses of ground-state properties [28], as well as MPS-based numerical simulations of our experimental protocol for both the simplified m-site blockaded model, described in Supplementary Information, and the full Hamiltonian (1). For the transitions into the $\mathbb{Z}_2$-ordered phase, some of the measured values of μ are slightly larger than the expected exponent from the Ising model and the nearest-neighbor blockade model, $\mu_{\text{Ising}} = 0.5$. We attribute these deviations, consistent with the MPS simulations of full Hamiltonian dynamics (see Supplementary Information), to a combination of the long-ranged interactions, finite-size and/or time ef-

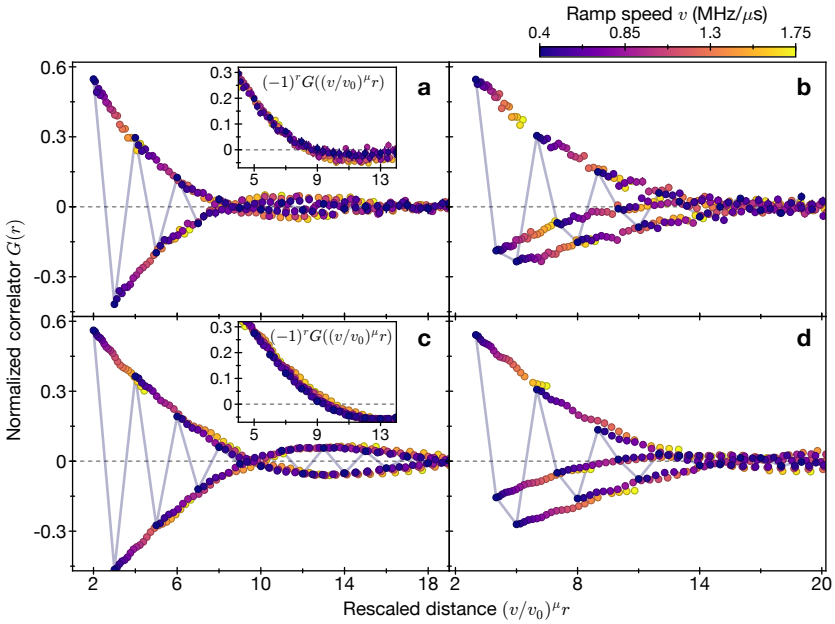

FIG. 3: **Universality of spatial correlations.** Collapse of the measured (**a**) and numerically calculated (**c**) correlations in the $\mathbb{Z}_2$-ordered phase with distances rescaled according to the experimentally observed scaling exponent. The blue line connects the points of the correlation function corresponding to the slowest sweep rate. The inset shows the staggered rescaled correlations. The negative values of the correlation function indicate nontrivial correlations between domain walls. Collapse of the measured (**b**) and numerically calculated (**d**) correlations in the $\mathbb{Z}_3$-ordered phase highlighting the energetic difference of the different types of defects, as shown by the distinguishability of the two negative branches, i.e., a deviation from a period-3 density wave. All error bars indicate the s.e.m.

fects [30], and systematic effects related to the inversion of the alternating pattern (Fig. 3a,c).

Quantum phase transitions associated with the breaking of a $\mathbb{Z}_3$ symmetry are more complex. They can belong to different universality classes, depending on the nature of the defects that can be formed. In our system, the defects correspond to two different types of domain walls, where the distance between neighboring Rydberg excitations is 2 sites and 4 sites (see Fig. 4a). For the experimentally accessible parameter regimes, the different associated excitation energies lead, in general, to an asymmetry between these defects (see also Fig. 4b). Correspondingly, the $\mathbb{Z}_3$-symmetry breaking is believed to be in the universality class of the 3-state *chiral* clock model (CCM) (Fig. 4a, Supplementary Information, and [28]).

The exact nature of such phase transitions has been a subject of intense theoretical research over the past three decades [14, 15, 28, 31, 32]. Only recently, theoretical analysis of equilibrium scaling properties [28] provided strong evidence for a direct transition between the ordered and disordered phases. In particular, finite-size scaling studies of a 2-site blockade model provides a QKZM exponent of $\mu \approx 0.37$ (see Supplementary Information and [28]), in good agreement with our measurements. Additional analysis of the correlations when $R_B \sim 2.43$ sites confirms the universal scaling behavior for the transition into the $\mathbb{Z}_3$-ordered phase (Fig. 3b). A striking feature of the collapsed data is that three branches are visible due to the fact that correlations at distances $3n+1$ are less prominent than those at distances $3n+2$. This is due to a strong preference for generating $\mathbb{Z}_4$-type domain walls, consistent with the chiral nature of the transition. We note that the chiral $\mathbb{Z}_3$ transition is the only known instance of a strongly coupled generic transition between gapped states in 1+1D with $z \neq 1$, implying an underlying nonconformal critical field theory [28]. The scaling collapse of the correlation growth (see Supplementary Information and Fig. S8) indeed indicates that our data are most consistent with $z > 1$.

The properties of the transition to a $\mathbb{Z}_4$-ordered phase are, at present, not fully understood theoretically. It is believed that in the 4-state CCM, there is no direct transition between the ordered and disordered phases, which are always separated by an intermediate gapless incommensurate phase [15, 31, 32]. Nonetheless, we find that our data in this region are reasonably consistent with power-law scaling with $\mu \sim 0.25$. This is in agreement with recent theoretical work showing that QKZM scaling may still hold on quenching through a gapless phase [33, 34], albeit with a modified (system-specific) power-law exponent [35]. While these considerations appear to be consistent with time-dependent MPS simula-

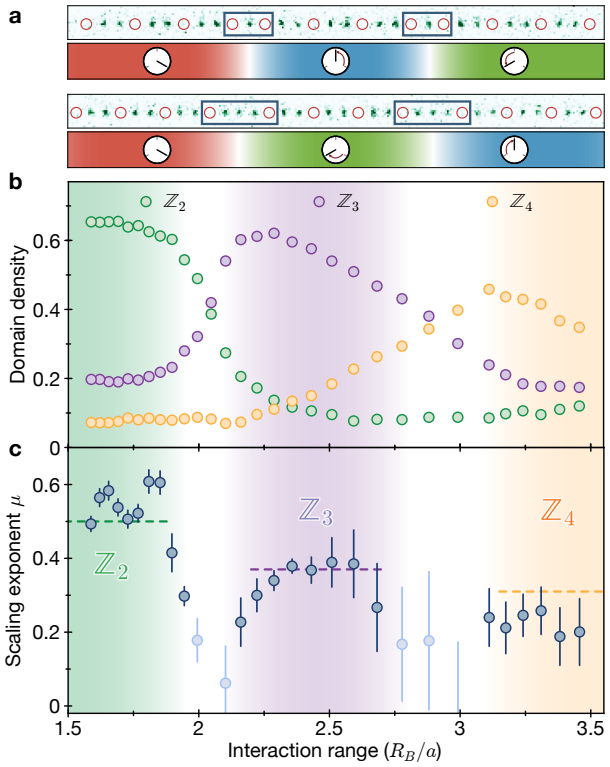

FIG. 4: **Power-law scaling for different interactions.** **a**, Experimental realization of the chiral clock model [28]. The top row shows a single fluorescence image of a state in the $\mathbb{Z}_3$-symmetry broken phase ($R_B/a \sim 2.22$), with two $\mathbb{Z}_2$-type defects displacing the Rydberg atoms in one direction. The bottom rows display a system with stronger interactions ($R_B/a \sim 2.43$), where $\mathbb{Z}_4$-type defects are favored, and the Rydberg atoms are displaced in the opposite direction. **b**, Fraction of the final state consistent with the different $\mathbb{Z}_N$-ordered states. Within the $\mathbb{Z}_3$-ordered region, the different type of defects appear with different probabilities and the most dominant type changes from $\mathbb{Z}_2$- to $\mathbb{Z}_4$-type as the interaction range increases. **c**, Measured scaling exponent, μ, as a function of R_B. Pale blue points indicate instances where the measured correlation lengths do not grow beyond the size of R_B. Shaded areas indicate the regions consistent with $\mathbb{Z}_2$- (green), $\mathbb{Z}_3$- (purple), and $\mathbb{Z}_4$-ordered (orange) phases. Dashed lines indicate the predictions from the equilibrium scaling properties of m-site blockade models (see Supplementary Information). Error bars represent the 68% confidence interval (b), and uncertainty of the power-law fit (c), which is dominated by systematic effects in the extraction of individual correlation lengths.

tions based on the 3-site blockade model (see Supplementary Information), detailed theoretical understanding of our experimentally observed exponents in the $\mathbb{Z}_4$ regime requires further studies. In particular, we note that quantitative numerical modeling of the dynamic sweeps into $\mathbb{Z}_3$- and $\mathbb{Z}_4$-ordered phases described by the Hamiltonian (1) using MPS yields higher values of μ (see SI). This comparison might be affected by finite-size effects, experimental imperfections, or accuracy of approximate numerical methods, highlighting the challenges associated with modeling complex, nonequilibrium quantum dynamics.

Our observations demonstrate a novel approach for probing quantum critical phenomena and provide new insights into the physics of exotic QPTs that do not lend themselves to simple theoretical analyses. Increasing the system size, improving atomic coherence properties, and exploring wider parameter regimes may allow for more precise probing of exotic QPTs into ordered phases as well as transitions into incommensurate phases [15, 29]. Two- and three-dimensional systems can also be explored using novel trapping techniques [36, 37]. A broader class of complex critical systems is accessible by introducing disorder in a controllable way, with local programmable detunings. Combining the present approach with time-dependent driving opens the door for studies of critical behavior in out-of-equilibrium quantum systems [38, 39], such as those undergoing dynamical phase transitions. Finally, the methods demonstrated in this work can be used to effectively encode and explore solutions to computationally difficult combinatorial optimization problems such as finding the Maximum Independent Set [40]. Detailed understanding of quantum dynamics in such systems might have direct applications for exploring quantum speedup in both adiabatic and dynamical quantum optimization algorithms [9].

ACKNOWLEGEMENTS

We thank Anushya Chandran, Eugene Demler, Anatoli Polkovnikov, and Ashvin Vishwanath for insightful discussions. This work was supported by NSF, CUA, ARO, AFOSR MURI, DOE, and Vannevar Bush Faculty Fellowship. A.O. acknowledges support by a research fellowship from the German Research Foundation (DFG). H.L. acknowledges support from the National Defense Science and Engineering Graduate (NDSEG) fellowship. S.S. acknowledges funding from the European Union under the Marie Skłodowska Curie Individual Fellowship Programme H2020-MSCA-IF-2014 (project number 658253). H.P. acknowledges support by the National Science Foundation (NSF) through a grant at the Institute of Theoretical Atomic Molecular and Optical Physics (ITAMP) at Harvard University and the Smithsonian Astrophysical Observatory. ME acknowledges funding provided by the Institute for Quantum Information and Matter, an NSF Physics Frontiers Center (NSF Grant PHY-1733907).

[1] Sachdev, S. *Quantum Phase Transitions* (Cambridge University Press, 2009), 2nd edn.

[2] Rüegg, Ch. *et al.* Quantum magnets under pressure: controlling elementary excitations in $TlCuCl_3$. *Phys. Rev. Lett.* **100**, 205701 (2008).

[3] Coldea, R. *et al.* Quantum criticality in an Ising chain: experimental evidence for emergeng E_8 symmetry. *Science* **327**, 177 (2010).

[4] Kibble, T. W. B. Topology of cosmic domains and strings. *J. Phys. A: Math. Gen.* **9**, 1387 (1976).

[5] Zurek, W. H. Cosmological experiments in superfluid helium? *Nature* **317**, 505 (1985).

[6] Chuang, I., Durrer, R., Turok, N. & Turke, B. Cosmology in the laboratory: Defect dynamics in liquid crystals. *Science* **251**, 1336 (1991).

[7] Bäuerle, C., Bunkov, Y. M., Fisher, S. N., Godfrin, H. & Picket, G. R. Laboratory simulation of cosmic string formation in the early Universe using superfluid ^{3}He. *Nature* **382**, 332 (1996).

[8] Ruutu, V. M. H. *et al.* Vortex formation in neutron-irradiated superfluid ^{3}He as an analogue of cosmological defect formation. *Nature* **382**, 334 (1996).

[9] Harrow, A. W. & Montanaro, A. Quantum computational supremacy. *Nature* **549**, 203 (2017).

[10] Polkovnikov, A., Sengupta, K., Silva, A. & Vengalattore, M. Colloquium: Nonequilibrium dynamics of closed interacting quantum systems. *Rev. Mod. Phys.* **83**, 863 (2011).

[11] Polkovnikov, A. Universal adiabatic dynamics in the vicinity of a quantum critical point. *Phys. Rev. B* **72**, 161201 (2005).

[12] Zurek, W. H., Dorner, U. & Zoller, P. Dynamics of a quantum phase transition. *Phys. Rev. Lett.* **95**, 105701 (2005).

[13] Dziarmaga, J. Dynamics of a quantum phase transition: Exact solution of the quantum Ising model. *Phys. Rev. Lett.* **95**, 245701 (2005).

[14] Huse, D. A. & Fisher, M. E. Domain Walls and the Melting of Commensurate Surface Phases. *Phys. Rev. Lett.* **49**, 793 (1982).

[15] Ostlund, S. Incommensurate and commensurate phases in asymmetric clock models. *Phys. Rev. B* **24**, 398 (1981).

[16] Harris, R. *et al.* Phase transitions in a programmable quantum spin glass simulator. *Science* **361**, 162 (2018).

[17] King, A. D. *et al.* Observation of topological phenomena in a programmable lattice of 1,800 qubits. *Nature* **560**, 456 (2018).

[18] Anquez, M. *et al.* Quantum Kibble-Zurek mechanism in a spin-1 Bose-Einstein condensate. *Phys. Rev. Lett.* **116**, 155301 (2016).

[19] Clark, L. W., Feng, L. & Chin, C. Universal space-time scaling symmetry in the dynamics of bosons across a quantum phase transition. *Science* **354**, 606 (2016).

[20] Endres, M. *et al.* The 'Higgs' amplitude mode at the two-dimensional superfluid/Mott insulator transition. *Nature* **487**, 454 (2012).

[21] Chen, D., White, M., Borries, C. & deMarco, B. Quantum quench of an atomic Mott insulator. *Phys. Rev. Lett.* **106**, 235304 (2011).

[22] Braun, S. *et al.* Emergence of coherence and the dynamics of quantum phase transitions. *PNAS* **112**, 3641 (2015).

[23] Bernien, H. *et al.* Probing many-body dynamics on a 51-atom quantum simulator. *Nature* **551**, 579 (2017).

[24] Jaksch, D. *et al.* Fast quantum gates for neutral atoms. *Phys. Rev. Lett.* **85**, 2208 (2000).

[25] Laguna, P. & Zurek, W. H. Critical dynamics of symmetry breaking: Quenches, dissipation, and cosmology. *Phys. Rev. D* **58**, 085021 (1998).

[26] Kolodrubetz, M., Clark, B. K. & Huse, D. A. Nonequilibrium dynamical critical scaling of the quantum Ising chain. *Phys. Rev. Lett.* **109**, 015701 (2012).

[27] Cherng, R. W. & Levitov, L. S. Entropy and correlation functions of a driven quantum spin chain. *Phys. Rev. A* **73**, 043614 (2006).

[28] Samajdar, R., Choi, S., Pichler, H., Lukin, M. D. & Sachdev, S. Numerical study of the chiral $\mathbb{Z}_3$ quantum phase transition in one spatial dimension. *Phys. Rev. A* **98**, 023614 (2018).

[29] Fendley, P., Sengupta, K. & Sachdev, S. Competing density-wave orders in a one-dimensional hard-boson model. *Phys. Rev. B* **69**, 075106 (2004).

[30] Jaschke, D., Maeda, K., Whalen, J. D., Wall, M. L. & Carr, L. D. Critical phenomena and Kibble-Zurek scaling in the long-range quantum Ising chain. *New. J. Phys.* **19**, 033032 (2017).

[31] Haldande, F. D. M., Bak, P. & Bohr, T. Phase diagrams of surface structures from Bethe-ansatz solutions of the quenatum sine-Gordon model. *Phys. Rev. B* **28**, 2743 (1983).

[32] Yeomans, J. ANNNI and clocj models. *Physica B+C* **127**, 187 (1984).

[33] Mondal, S., Sen, D. & Sengupta, K. Quench dynamics and defect production in the Kitaev and extended Kitaev models. *Phys. Rev. B* **78**, 045101 (2008).

[34] Divakran, U., Dutta, A. & Sen, D. Landau-Zener problem with waiting at the minimum gap and related quench dynamics of a many-body system. *Phys. Rev. B* **81**, 054306 (2010).

[35] Dutta, A. *et al. Quantum phase transitions in transverse field spin models: From Statistical Physics to Quantum Information* (Cambridge University Press, 2015).

[36] Barredo, D., Lienhard, V., de Léséleuc, S., Lahaye, T. & Browaeys, A. Synthetic three-dimensional atomic structures assembled atom by atom. *Nature* **561**, 79 (2018)

[37] Kumar, A., Wu, T.-Y., Giraldo Mejia, F. & Weiss, D. S. Sorting ultracold atoms in a three-dimensional optical lattice in a realization of Maxwell's demon. *Nature* **561**, 83 (2018)

[38] Erne, S., Bücker, R., Gasenzer, T., Berges, J. & Schmiedmayer, J Observation of universal dynamics in an isolated one-dimensional Bose gas far from quilibrium. *arXiv:1805.12310* (2018).

[39] Prüfer, M. *et al.* Observation of universal quantum dynamics far from equilibrium. *arXiv:1805.11881* (2018).

[40] Pichler, H., Wang, S.-T., Zhou, L., Choi, S. & Lukin, M. D. Quantum Optimization for Maximum Independent Set Using Rydberg Atom Arrays. *arXiv:1808.10816* (2018).

SUPPLEMENTARY INFORMATION

Rydberg array preparation. The experiment utilizes an acousto-optic deflector to generate multiple optical tweezers, which are loaded probabilistically from a cold gas of ^{87}Rb atoms in a magneto-optical trap. Each tweezer can be loaded with up to a single atom. Once the cloud is dispersed, a fluorescence image, similar to the ones shown in Fig. 2a of the main text, is taken to identify loaded traps. The traps are then rearranged to generate a defect-free regular array of atoms, evenly separated by a distance a [41].

We define our spin Hamiltonian according to two pseudospin-1/2 states. The first is a ground-state hyperfine sublevel, $|g\rangle = |5S_{1/2}, F = 2, m_F = -2\rangle$. The second is the interacting Rydberg state $|r\rangle = |70S, J = 1/2, m_J = -1/2\rangle$. These two states are coupled by a two-photon process via the intermediate state $|e\rangle = |6P_{3/2}, F = 3, m_F = -3\rangle$. The two lasers operate at wavelengths 420 nm for the lower transition and 1013 nm for the upper transition.

The 420 nm laser is a frequency-doubled Titanium-Sapphire laser (SolsTiS 4000 PSX F by M Squared), locked to an optical reference cavity (ATF- 6010-4 from Stable Laser Systems). The 1013 nm laser is an external cavity diode laser (CEL002 by MOGLabs) that is locked to the same reference cavity. The transmitted light through the cavity is used to injection lock another 1013 nm laser diode, which is then amplified by a tapered amplifier [42].

Both beams are focused along the array axis (aligned with the quantization axis) to drive σ^- and σ^+ transitions for the 420 nm and 1013 nm beams, respectively.

Pulse generation. We modulate the 420 nm Rydberg laser with an AOM driven by an arbitrary waveform generator (AWG, M4i.6631-x8 by Spectrum Instrumentation). For each experiment, we program a waveform with varying amplitudes, frequencies and phases in the time domain into the AWG, which is then transmitted to the AOM through a high-power RF amplifier (ZHL-1-2W+ by Mini-Circuits).

The nonlinear AOM response to changes in amplitude and frequency poses a technical challenge. The deflection efficiency is not proportional to the waveform amplitude, and large changes in the waveform frequency lead to variations in the deflection efficiency. These effects lead to distortions in the pulse shape. We apply feed-forward corrections to the amplitude to both match the output intensity to the desired waveform amplitude, as well as to compensate for the variations with frequency.

Pulse Parameters. All pulses begin by turning on the value of Ω linearly over 1 μs at a fixed initial detuning Δ_0. We select our initial detuning to be as close to the critical point as possible subject to the constraint that the initial turn-on is still fully adiabatic. We identify this detuning experimentally by ramping Ω on and then off for various fixed detunings. In the adiabatic case, all the atoms should return to $|g\rangle$. We therefore select the detuning closest to resonance that still shows no excess excitation at the end of the pulse. For a typical measurement in the $\mathbb{Z}_2$ regime, we select $\Delta_0 = -2.5$ MHz (Fig. S1).

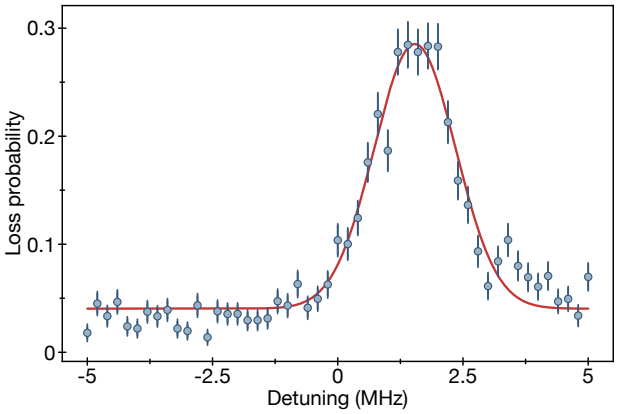

Figure S1: **Determination of Δ_0.** At a fixed laser detuning, we linearly ramp Ω on and then off over 1 μs each. We identify the negative detuning closest to resonance for which we are fully adiabatic, such that the excitation probability at the end of the pulse returns to the minimum. From this typical measurement, taken at $R_B/a = 1.59$, we set $\Delta_0 = -2.5$ MHz.

The final detunings of the sweeps are chosen in most cases to cross the tip of the corresponding phase boundary. In some cases in which the interaction strength is on the border between two phases, we do not fully cross over the boundary (Fig. S2a).

The power-law scaling behavior of the correlation length can be limited owing to strong nonadiabaticity far away from the critical point, where the behavior of the system is susceptible to the microscopic details and should deviate from universal theories, limiting how fast a sweep across the phase transition can be. At the same time, slow sweeps are more susceptible to decoherence, both because of the longer pulse time window, and because the system remains closer to the ground state near the critical point and the growing quantum correlations are increasingly sensitive to environmental noise. To determine the range of rates for which QKZM scaling can be observed, we perform a sweep into each of the ordered phases at a wide range of sweep speeds v. We fit the correlation lengths for each parameter, discarding all the instances where the correlation length is smaller than the size of the blockade radius, to a model that accounts for incoherent processes as a saturation in the final size of

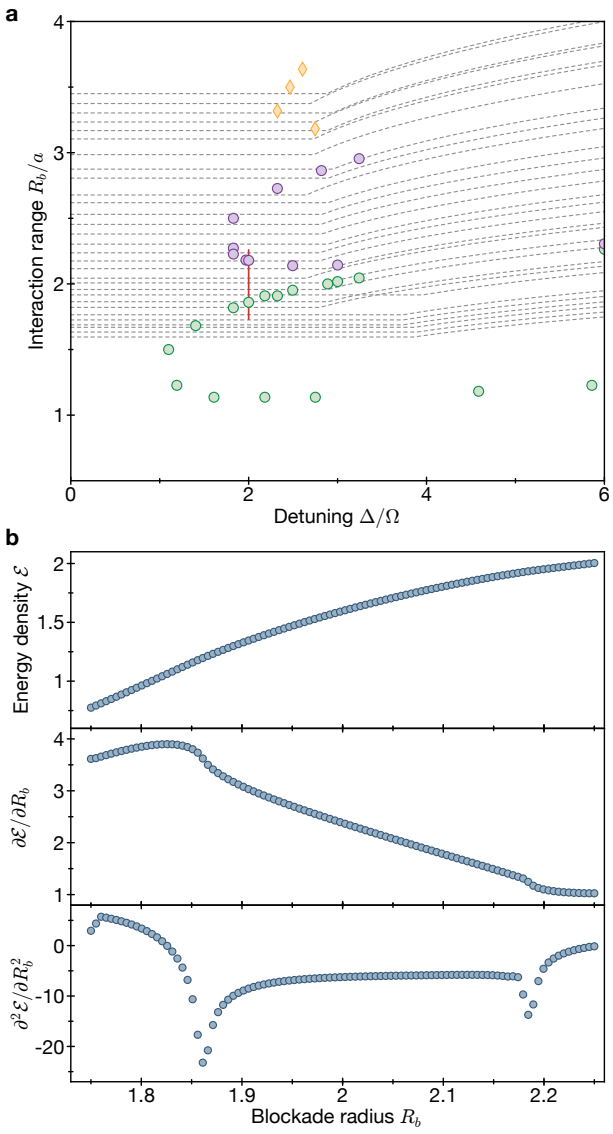

Figure S2: **Numerically extracted phase diagram with trajectories for QKZM measurements. a**, Green (purple) markers indicate the phase boundary points between disordered and $\mathbb{Z}_2$-($\mathbb{Z}_3$-)ordered phases. Yellow diamonds indicate the boundaries of the disordered phase (as approached from increasing Δ with fixed Ω and R_b). We have not verified if these transitions are directly from disordered to $\mathbb{Z}_4$-ordered phases, or involve incommensurate phases. Each gray dashed line corresponds to the trajectory across phase space used to probe for scaling behavior of correlation length growth. The horizontal section of each trace corresponds to the detuning sweep at a constant Rabi frequency, while the curved sections correspond to pulse turn-off at a fixed value of the detuning. The total duration of the detuning sweep is varied to control the rate of transition across the phase boundaries, but the time to turn the field off is not. **b**, Numerically obtained energy densities $\mathcal{E}$ along the red solid line indicated in **(a)**. The second order derivatives of $\mathcal{E}$ shows clear cusps at two critical points.

the correlation length, namely:

$$\xi(v) = \begin{cases} \xi_0(v_0/v)^\mu & : v \le v_c, \\ \xi_0(v_0/v_c)^\mu & : v > v_c. \end{cases} \tag{3}$$

From this fit, we set $v_{\min} > v_c$ and find $v_{\max}$ such that $\xi(v_{\max}) > R_B$. An example of this can be seen in Fig. S3. In this way, we determine the sweep parameters for the different values of the interaction strength (see Table 1).

Numerical computation of the phase diagram. The quantum critical points along the phase boundary on the phase diagram presented in the main text were obtained using both finite- and infinite-system density-matrix renormalization group (DMRG) algorithms [43–48]. The filled colored regions are not the result of numerical simulations, and only show approximately the expected shape of the phases. In this section, we describe the details of the DMRG calculations.

For the infinite-system DMRG (iDMRG), we generally follow the method summarized in Ref. [49], where translationally invariant matrix product states (iMPS) are used as variational ansatze for ground-state wavefunctions. Our Hamiltonian with long-range interactions is encoded using matrix product operator representations, where $1/r^6$ decaying interactions are approximated by a linear combination of four exponentials

$$\frac{1}{r^6} \approx \sum_{i=1}^{4} c_i x_i^r, \tag{4}$$

with $(c_1, c_2, c_3, c_4) = (170.55, 1.29, 0.0252, 0.000279)$ and $(x_1, x_2, x_3, x_4) = (0.00519, 0.0835, 0.279, 0.565)$ [50]. The resultant function provides an excellent approximation with relative error less than 10^{-5} (Fig. S4). This accuracy implies that even with the strongest interaction strength probed in our experiments ($R_b \approx 3.5$), the maximum correction, $V_0 \left| 1/r^6 - \sum_{i=1}^4 c_i x_i^r \right| \lesssim (2\pi) \times 36$ kHz, is much weaker than the smallest energy scale that can be probed within our experimental timescales.

Our phase diagram involves quantum phases that spontaneously break spatial translation symmetry. Hence, it is important that the number of spins in a translationally invariant unit cell of our iMPS ansatz must be compatible with the broken spatial symmetry. We use 2 or 6 spins as a unit cell in order to probe phase transitions from disordered to $\mathbb{Z}_2$-ordered or $\mathbb{Z}_3$-ordered phases, respectively. Incommensurate phases or onset of spatial symmetry breaking that is not compatible with the number of spins per unit cell can be identified by oscillatory behavior of wavefunction overlaps or energy densities over iterations.

In order to obtain the ground-state wavefunction, we iteratively optimize iMPS tensors until the (local) overlap

R_B/a	Δ_f [MHz]	Δ_0 [MHz]	$v_{\min}$ [MHz/μs]	$v_{\max}$ [MHz/μs]
1.58	7.5	-2.5	3.5	15.2
1.62	7.5	-2.5	3.5	15.2
1.65	7.5	-2.5	3.5	15.2
1.69	7.5	-2.5	3.5	15.2
1.72	7.5	-2.5	3.5	15.2
1.76	7.5	-2.5	3.5	15.2
1.81	5.5	-2.5	4.6	19.7
1.85	5.7	-2.3	4.6	19.7
1.89	7.6	-2.4	3.5	15.2
1.94	5.7	-2.3	4.6	19.7
1.99	5.7	-2.3	4.6	19.7
2.04	5.3	-2.7	4.6	19.7
2.10	5.7	-2.3	4.6	19.7
2.16	5.5	-2.5	4.6	19.7
2.22	5.5	-2.5	4.6	19.7
2.28	5.7	-2.3	4.6	19.7
2.35	5.5	-2.5	4.6	19.7
2.43	5.4	-2.6	4.6	19.7
2.50	5.5	-2.5	4.6	19.7
2.59	5.6	-2.4	4.6	19.7
2.68	5.3	-2.7	4.6	19.7
2.77	5.6	-2.4	4.6	19.7
2.88	5.9	-2.1	4.6	19.7
2.99	5.5	-2.5	4.6	19.7
3.11	5.5	-2.5	4.6	19.7
3.17	5.8	-2.2	4.6	19.7
3.24	5.5	-2.5	4.6	19.7
3.31	5.9	-2.1	4.6	19.7
3.38	5.4	-2.6	4.6	19.7
3.45	5.8	-2.2	4.6	19.7

Table 1: **Pulse parameters for QKZM sweeps**

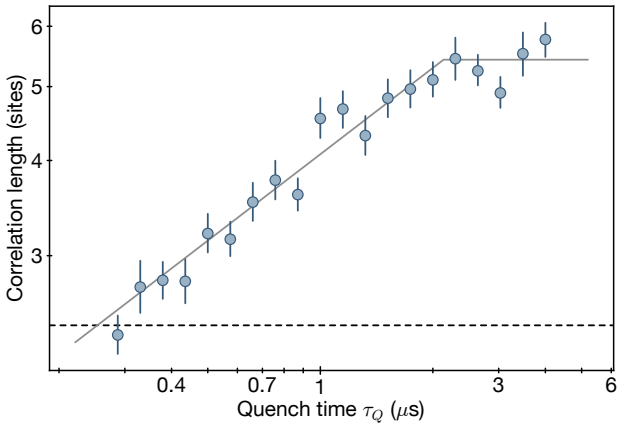

Figure S3: **Scaling window.** Determination of the window of rates where scaling is valid for the transition into the $\mathbb{Z}_3$-ordered phase. The black solid lines represent the result of the fitted model which grows as a power law until it saturates. The dashed horizontal line marks the size of the blockade radius. The values of all the rates used in the experiment are larger than the value at which the dashed and solid lines intersect, and smaller than the point where the model saturates.

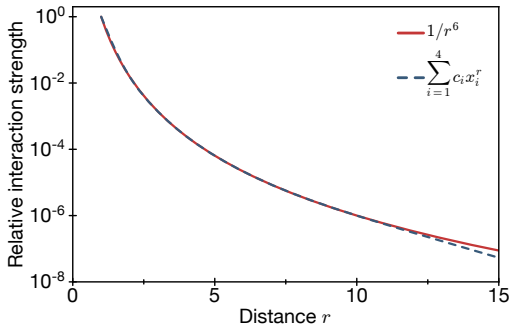

Figure S4: **Interaction potential approximation.** Comparison between the exact power-law decay $1/r^6$ and its approximation using a linear combination of four exponentials. The two functions agree with each other until their relative strength decreases to 10^{-6}.

between wavefunctions from two consecutive optimization steps approaches unity up to a small error ϵ. As convergence criteria, we require that either $\epsilon \leq 10^{-8}$ or ϵ is limited by truncation errors arising from finite bond dimension D [49]. We use a wide range of bond dimensions up to $D = 200$, depending on the quantity of interest to be computed and on the convergence of wavefunctions. For example, computing the ground state energy density is relatively insensitive to bond dimensions, while extracting correlation lengths near the critical point requires a substantially larger D.

We thus extract the phase boundaries from the energy density. More specifically, we use iDMRG to extract the ground-state energy density $\mathcal{E}$ along a line in the parameter space, $(R_b, \Delta/\Omega)$, and compute its second derivative along the line. When crossing a quantum phase transition, the second-order derivative of the energy density exhibits a sharp feature. For example, Fig. S2b shows the numerically computed energy densities per unit cell (6 spins) as a function of $R_b \in [1.75, 2.25]$ for a fixed $\Delta/\Omega = 2$ with $D = 10$. We find clear cusps at $R_b \approx 1.86$ and 2.18, corresponding to critical points from $\mathbb{Z}_2$-ordered to disordered and to $\mathbb{Z}_3$-ordered phases. Similar procedures along different lines lead to the phase diagram in Fig. S2a and in Fig. 1c of the main text.

These phase boundaries are also reproduced using finite-system DMRG [51, 52] with a bond dimension up to $D = 60$ for a chain of $L = 51$ atoms and open boundary conditions. The first three energy levels are individually targeted, which, in turn, gives us access to the energy gap. The closing of the gap outlines well-defined lobes in the phase diagram, the boundaries of which overlap well

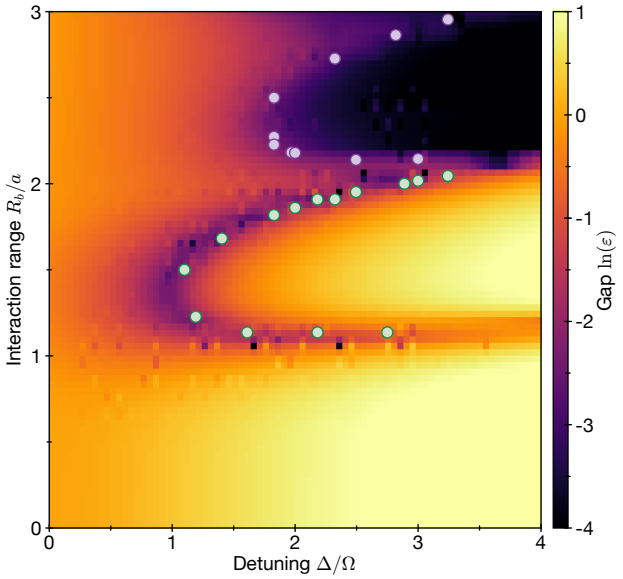

Figure S5: **Energy gap.** Calculated gap between ground and first excited state using DMRG. Green (purple) circles indicate the extracted QCP separating the disordered from the $\mathbb{Z}_2(\mathbb{Z}_3)$-ordered phase.

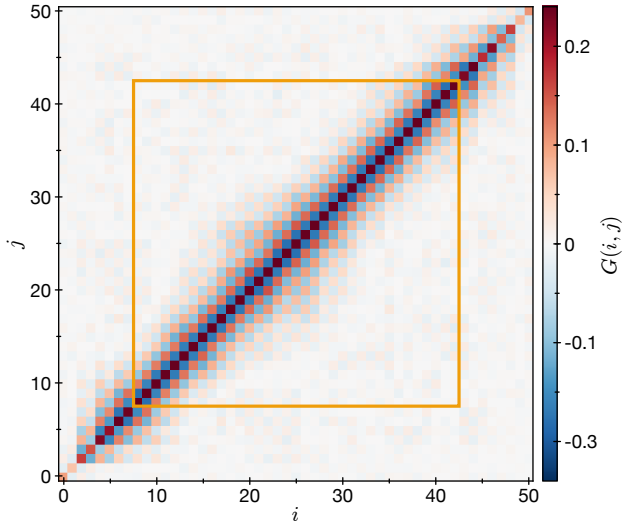

Figure S6: **Rydberg density-density correlations.** Full density-density correlation map for sites i and j after a slow sweep into the $\mathbb{Z}_2$-ordered phase. The orange square outline marks the bulk region used for analysis.

with the points extracted previously with iDMRG (see Fig. S5).

A few remarks are in order. First, it has been previously discussed that the $\mathbb{Z}_3$-ordered phase may be interfacing incommensurate phases [29]. However, we do not find any evidence of incommensurate phases between $\mathbb{Z}_2$ and $\mathbb{Z}_3$ phases up to $\Delta/\Omega = 12$ within our numerical precision. The nature of the direct transition from disordered to $\mathbb{Z}_3$-ordered phases is discussed in Refs. [28, 53, 54]. Second, we have not explicitly identified the phase transition between disordered to $\mathbb{Z}_4$-ordered phases. This is because our choices of a unit cell (two or six spins) are not compatible with $\mathbb{Z}_4$-ordered wavefunctions. Instead, the boundary of the disordered phase for $R_b > 3$ (yellow diamonds in Fig. S2a) has been extracted from the convergence of the iDMRG algorithm; as Δ/Ω increases with a fixed R_b, the yellow diamonds in Fig. S2a indicate the critical points at which the iDMRG algorithm ceases to converge, and instead exhibits oscillatory behaviors. Our method does not distinguish whether this is due to the onset of the $\mathbb{Z}_4$-ordered phase or a gapless incommensurate phase.

Correlation length extraction and scaling. From the fluorescence pictures obtained at the end of an experimental sequence, we calculate the two-dimensional Rydberg density-density correlation map:

$$G(i,j) = \langle n_i n_j \rangle - \langle n_i \rangle \langle n_j \rangle. \tag{5}$$

To minimize boundary effects, we disregard 8 sites from each edge. From the remaining bulk correlations, we average out this map over diagonal lines of constant $|i-j|$ to obtain the Rydberg density-density correlation described in Eq. (2) in the main text (Fig. S6). The uncertainties for the values of $G(r)$ are found via a jackknife analysis.

Two different approaches are used to extract a characteristic length from such correlations. For transitions into $\mathbb{Z}_N$-ordered states (Fig. 4), we perform a least squares fit to the data with the model function:

$$\hat{G}(r) = Ae^{-r/\xi}\hat{G}_N(r)_{\text{gs}}, \tag{6}$$

where A is the amplitude at $r = 0$, ξ is the correlation length, and $\hat{G}_N(r)_{\text{gs}}$ is the ideal correlation function at integer values of r for the corresponding $\mathbb{Z}_N$-ordered state, with a peak every N sites:

$$\begin{aligned} \hat{G}_2(r)_{\text{gs}} &= \cos(2\pi r/2) \\ \hat{G}_3(r)_{\text{gs}} &= \cos(2\pi r/3) \\ \hat{G}_4(r)_{\text{gs}} &= \cos(2\pi r/4) + 1/2\cos(2\pi r/2). \end{aligned} \tag{7}$$

The range of distances used for all fits is $0 < r \leq 20$, where the cutoff at 20 sites is used to avoid any potential finite-size effects of the system.

In addition to the procedure described above, for $\mathbb{Z}_2$-ordered states it is possible to extract a correlation length by fitting an exponential decay to the modulus of the correlation function, as is done in Fig. 2 of the main text. This method allows for the determination of the correlation length in a way that is less susceptible to systematic effects arising from inversions of the alternating

pattern, as observed in Fig. 3a of the main text. However, this method cannot be applied to $\mathbb{Z}_N$-ordered states for $N > 2$, necessitating the use of a more general approach, such as the function $\hat{G}(r)$ defined above. While the scaling exponents extracted using both of these methods for the $\mathbb{Z}_2$-ordered state data are consistent within error bars, $\hat{G}(r)$ is used to obtain all exponents in Fig. 4c of the main text.

To extract the most likely scaling exponent μ at a given interaction, we fit a power law

$$\xi = \xi_0 \, (v/v_0)^{-\mu}, \tag{8}$$

where v is the detuning sweep rate.

$\mathbb{Z}_N$ domain density. In the fluorescence images obtained at the end of each experimental sequence, we identify the loss of an atom to a Rydberg excitation. In this way, we can directly count the number of instances of two lost atoms separated by N sites, where every site in between contains an atom. To extract the data for Fig. 4b in the main text, we disregard the first 8 sites from the edges and count the instances in which both ends of the N atom chain are within the bulk, f_N. The relative probability for two lost atoms separated by N sites is given by:

$$p_N = \frac{N \times f_N}{\sum_{i>0}(i \times f_i)}. \tag{9}$$

Unlike $G(r)$, p_N is susceptible to detection infidelity [23, 42].

Length rescaling of correlation functions. In Fig. 3 of the main text, we use the normalized measured density-density correlation functions, $\frac{1}{A_i}G(r)_i$, and rescale the length r by the QKZM length scaling exponent found via the scaling analysis of correlation length, $r \rightarrow (v/v_0)^{\mu} r$.

Finite-time scaling. The length scaling exponent, μ, found experimentally sets constraints to the possible combinations of the critical exponents z and ν at a given interaction strength. In order to estimate, or qualitatively test, the possible values of z and ν, given the constraints set by μ, we make use of the fact that in the critical region, all system properties scale in a universal way. The QKZM predicts a universal scaling of time with a scaling exponent of $z\nu/(1+z\nu)$, in addition to the scaling of length with $\mu = \nu/(1+z\nu)$ [55] . In the experiment, the control parameter used to cross the quantum phase transition is $\delta = \Delta - \Delta_c$, where Δ_c is the value of the detuning at the critical point and can be estimated through numerical simulations (see section on numerical computation of the phase diagram). Near the critical point, the control parameter varies in time as $\delta(t) = vt$, leading to a universal scaling of $\delta(v) = \delta_0(v_0/v)^{\kappa}$, where

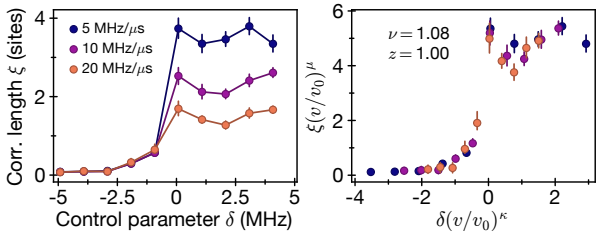

Figure S7: **Finite-size scaling across QPT into $\mathbb{Z}_2$-ordered phase.** Verification of critical exponents across the QPT into $\mathbb{Z}_2$-ordered phase by rescaling the control parameter and spatial correlations. Using the experimentally extracted value of the QKZM length scaling exponent, $\mu = 0.52$, and setting the dynamical critical exponent to the Ising prediction, $z = 1$, it is observed that the data falls along a smooth function.

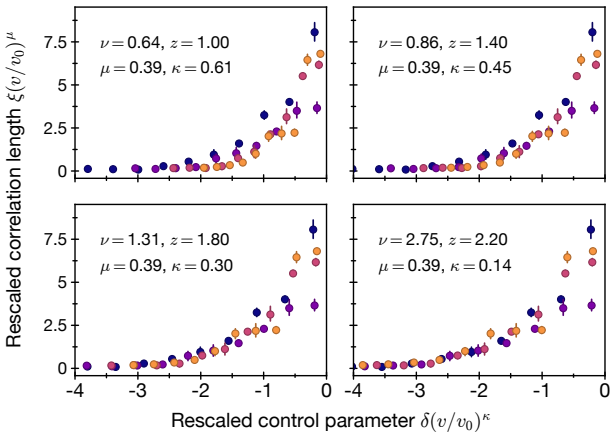

Figure S8: **Finite-size scaling across QPT into $\mathbb{Z}_3$-ordered phase.** Verification of critical exponents across the QPT into $\mathbb{Z}_3$-ordered phase by rescaling the control parameter and spatial correlations. Using the experimentally extracted value of QKZM length scaling exponent, $\mu = 0.39$, the dynamical critical exponent is varied from $z = 1$ to $z = 2.2$. The data collapse is most consistent with a dynamical critical exponent of $z > 1$, confirming that the phase transition corresponds to a nonconformal field theory.

$\kappa = -1/(1+z\nu)$. Using the data shown in the main text for the correlation length growth across the transition into the $\mathbb{Z}_2$-ordered phase, we can apply the transformation $\xi \rightarrow \xi(v/v_0)^{\mu}$ and $\delta \rightarrow \delta(v/v_0)^{\kappa}$, to observe how well the data collapses to a universal shape. Fig. S7 shows that these data are consistent with having critical exponents $z = 1 \simeq \nu$, as is expected for the Ising universality class. Applying the same methods to the transition into the $\mathbb{Z}_3$-ordered phase shows that the data collapse best for values of $z > 1$ (Fig. S8), qualitatively consistent with theoretical predictions of an underlying nonconfor-

mal field theory for the transition into this phase.

Numerical simulation of Kibble-Zurek dynamics. We numerically model the dynamics of the system using matrix product states and employ a variant of a time evolving block decimation (TEBD) algorithm to propagate the state. We use a state update that allows us to exactly include the effect of interaction between atoms that are separated by less than $\ell = 7$ sites. Interactions beyond this range are neglected. To this end, we use a Trotterization for the unitary that propagates the system from a time t_k to a time $t_{k+1} = t_k + \Delta t$ as

$$U(t_k \to t_{k+1}) \approx \prod_{p=1}^{N-\ell} \exp\left(-i h_p(t_k)\Delta t\right), \tag{10}$$

where

$$\begin{aligned} h_p(t_k) = \; & \frac{1}{\ell}\sum_{j=0}^{\ell-1}\left(\frac{\Omega(t_k)}{2}\sigma^x_{p+j} - \Delta(t_k) n_{p+j}\right) \\ + \; & \sum_{i=0}^{\ell-2}\sum_{j=i+1}^{\ell-1}\frac{1}{\ell-(j-i)} V_{i,j} n_{p+i} n_{p+j} \end{aligned} \tag{11}$$

for $1 < p < N-\ell$, and h_1 and $h_{N-\ell}$ are similar, but with appropriately adjusted coefficients.

We simulate the evolution according to the same pulse shape as applied in the experiment, with a time step of $\Delta t = 0.15$ ns and a bond dimension of 128. A comparison between the numerically simulated dynamics and the experimental results for different interaction strengths is shown in Fig. S9. As described in the section on "Correlation length extraction and scaling", deviations of the individual correlation functions from an exponentially decaying period-N density wave lead to systematic effects that dominate the uncertainty in the determination of the values presented in Fig. S9b. The comparison between experimental and numerical results is susceptible to multiple effects, including finite-size effects, accuracy of the approximate numerical methods used, experimental imperfections, and data fitting, which contribute to the observed discrepancy.

m-site blockade model. The $\mathbb{Z}_n$-symmetry-breaking QPTs observed in the Rydberg atom array are mirrored in the $(n-1)$-site blockade model. To be precise, consider the Hamiltonian

$$H_{\text{Ryd}} = \sum_{i=1}^{N}\frac{\Omega}{2}(|g\rangle_i\langle r| + |r\rangle_i\langle g|) - \Delta n_i + \sum_{x\geq 1} V_x n_i\, n_{i+x}. \tag{12}$$

In the limit $V_x \to \infty \; \forall\, x \leq m$ and $V_x = 0$ for $x > m$, this defines the so-called m-site blockade model [23, 29]. In this model, interactions between neighboring Rydberg atoms are so strong as to completely prevent the occupation of up to the nearest m sites, and are negligible for larger distances. In other words, all states obey the m-site blockade constraint:

$$n_i\, n_{i+x} = 0, \; \forall\, x \leq m. \tag{13}$$

With $\Delta \gg \Omega$ and m sites blockaded, in the (perfectly) ordered phase, the system maximizes the density of Rydberg atoms by having one excitation every $(m+1)$ sites. The resulting ordered state thus breaks a $\mathbb{Z}_n$ symmetry for $n = m+1$, akin to the Rydberg array. For m=1 this model is closely linked to the quantum dimer models [56].

Our analysis of the critical properties of the m-site blockade model in this section is based on finite-size scaling (FSS) [57, 58]. Near the quantum critical point (QCP), the energy gap ε is assumed to obey a scaling ansatz of the functional form

$$\frac{\varepsilon}{\Omega} = N^{-z}\,\mathcal{F}\left(N^{1/\nu}\,\frac{(\Delta - \Delta_c)}{\Omega}\right), \tag{14}$$

for some universal scaling function $\mathcal{F}$. In order to pinpoint the location of the QPT, we plot $(\varepsilon/\Omega)\,N^z$ against the tuning parameter Δ/Ω for various lattice sizes and values of z (Fig. S10a). Precisely at the QCP $\Delta = \Delta_c$, the combined variable $(\varepsilon/\Omega)\,N^z$ is independent of the length of the system N according to Eq. (14). Therefore, with the correct choice of z, all the curves for $(\varepsilon/\Omega)\,N^z$, corresponding to different values of N, should cross at Δ_c. This enables us to both determine the QCP Δ_c *and* estimate the value of z simultaneously. Similarly, Eq. (14) predicts that on plotting $(\varepsilon/\Omega)\,N^z$ against $N^{1/\nu}\,(\Delta - \Delta_c)/\Omega$, the resulting curves should ideally merge into a single one for different system sizes. This data collapse, illustrated in Fig. S10b, occurs for a value of $\nu = 1$, 0.71, and 0.57 for the $\mathbb{Z}_2$, $\mathbb{Z}_3$, and $\mathbb{Z}_4$ transitions, respectively.

With the knowledge of the values of z and ν, we can test the Kibble-Zurek prediction for the creation of domain walls when the system is quenched across a phase transition. Deep in the ordered phase, the number of domain walls in the m-site blockade model is simply related to the number of Rydberg excitations. We thus define the domain wall density as

$$d = \frac{1}{m+1}\left(1 - (m+1)\sum_i \frac{\langle n_i\rangle}{N}\right). \tag{15}$$

Since the domain wall density is inversely proportional to the correlation length $d \sim \xi^{-1}$, the Kibble-Zurek argument predicts a scaling of the correlation length as $d \sim \tau^{-\nu/(1+z\nu)}$. The numerical results obtained from a time dependent matrix product state simulation of the m-site blockade model, shown in Fig. S11, agree well with this prediction according to the exponents extracted above from the finite-size scaling analysis, i.e. $\mu = 0.5$, 0.37, and 0.29 for $m = 1$, 2 and 3.

Chiral clock models. QPTs in the Rydberg Hamiltonian, Eq. (1) of the main text, involving $\mathbb{Z}_n$ ($n \geq 3$)

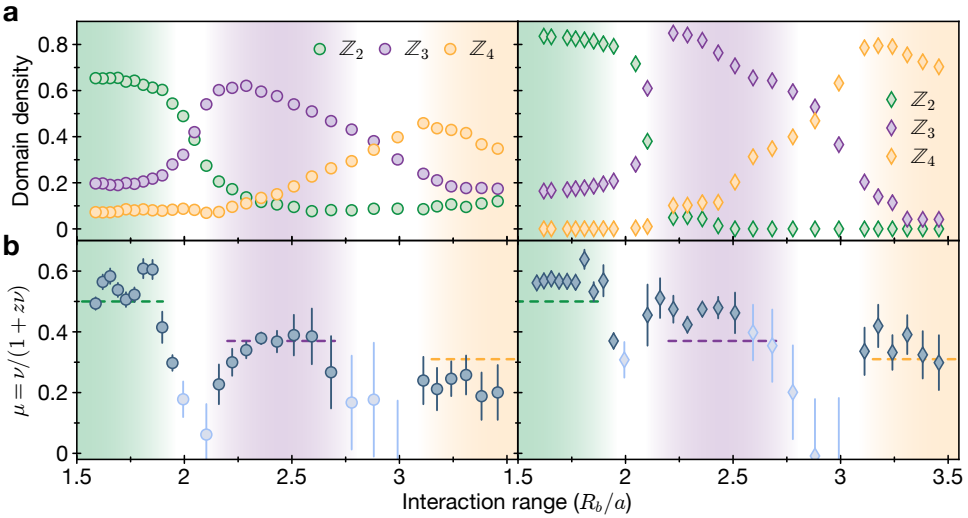

Figure S9: **MPS simulation of system dynamics.** Comparison of experimental results from Fig. 4 of the main text (left column, circles) to MPS (right column, diamonds). MPS simulations use experimental parameters to extract relative order (**a**) after slow sweeps. Detection errors are not accounted for in the MPS data which leads to a higher contrast. **b**, Comparison of extracted scaling exponents for experimental (circles) and MPS (diamonds) data. Pale blue dots indicate instances where the correlation length is smaller than the blockade radius. The error bars denote the uncertainty of the power-law fit, which is dominated by systematic effects in the extraction of individual correlation lengths.

translational symmetry breaking along one spatial direction are expected to be in the universality class of the extensively-studied $\mathbb{Z}_n$ *chiral* clock models [14, 15, 31, 59–62]. To elucidate this connection, let us focus on $n = 3$ and consider the case when $V_1 \gg |\Omega|, |\Delta|$, that is, nearest-neighbor interactions are strong enough to effectively preclude two neighboring atoms from simultaneously being in the Rydberg state. Since the van der Waals interactions decay rapidly as $V_x = C_6/x^6$, we neglect couplings beyond the third-nearest neighbor by approximating $V_x \approx 0$ for $x \geq 3$, leading to a truncated model of the form:

$$H_{\rm Ryd} = \sum_{i=1}^{N} \frac{\Omega}{2}(|g\rangle_i\langle r| + |r\rangle_i\langle g|) - \Delta n_i + V_2 n_i n_{i+2}, \tag{16}$$

supplemented with the constraint $n_i\, n_{i+1} = 0$.

The Hamiltonian (16) can be mapped to a system of hard-core bosons, where no more than one boson can occupy a single site. This follows upon identifying the state where the atom at site i is in the internal state $|r\rangle$ ($|g\rangle$) with the presence (absence) of a boson. Defining the bosonic annihilation and number operators, b_i and $n_i = b_i^\dagger b_i$, respectively, we obtain

$$H_b = \sum_{i=1}^{N} \frac{\Omega}{2}\,(b_i^\dagger + b_i) - \Delta n_i + V_2\, n_i n_{i+2}, \tag{17}$$

together with $n_i\, n_{i+1} = 0$. This model (often referred to as the $U-V$ model) was shown by Refs. [29, 63] to exhibit a phase transition in the universality class of the three-state chiral clock model (CCM), over a set of parameters.

The $\mathbb{Z}_n$ CCM is a simple extension of the transverse-field Ising model in which each spin is promoted to have $n > 2$ states. However, instead of extending the symmetry from $\mathbb{Z}_2$ to $\mathbb{S}_n$, which would result in the n-state Potts model [64], the interactions are constructed to be invariant under $\mathbb{Z}_n$ transformations. With $n = 3$, the three-state CCM is defined by the Hamiltonian [61, 62]

$$H_{\rm CCM} = -f \sum_{j=1}^{N} \tau_j^\dagger\, \mathrm{e}^{-\mathrm{i}\,\phi} - J \sum_{j=1}^{N-1} \sigma_j^\dagger\, \sigma_{j+1}\, \mathrm{e}^{-\mathrm{i}\,\theta} + \mathrm{h.c.} \tag{18}$$

acting on a one-dimensional chain of N spins. The three-state spin operators τ_i and σ_i, which can be represented

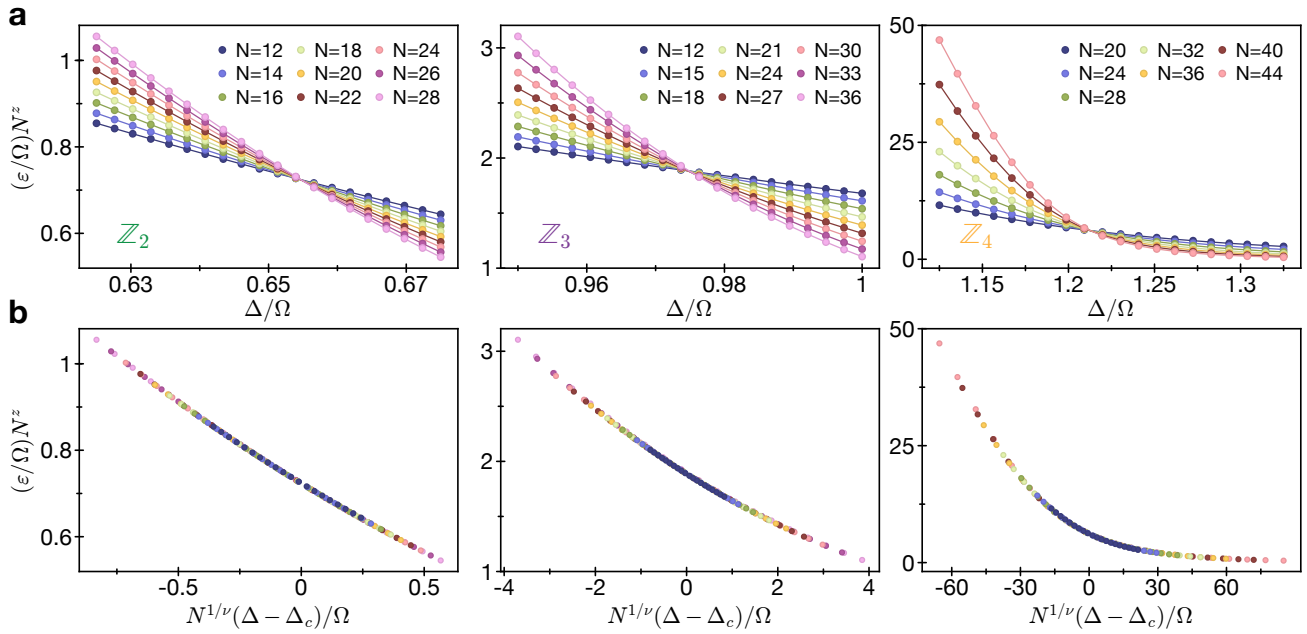

Figure S10: **Finite-size scaling analysis of the m-site blockade model. a,** We show the energy gap, ε, between the ground state and the first excited state for $m = 1$ (left), $m = 2$ (middle) and $m = 3$ (right). As one can see, the energy gap becomes independent of system size at a point Δ_c/Ω, if rescaled with a factor N^z. For $m = 1$, 2, and 3, this happens at $\Delta_c/\Omega = 0.6548$, 0.9745, and 1.213 with $z = 1$, 1.33 and 1.70, respectively. Data is obtained by exact diagonalization of a system of N atoms with periodic boundary conditions. **b**, The data collapses on a single universal function if the x-axis is rescaled by a factor $N^{1/\nu}$ with $\nu = 1$, 0.71 and 0.57 for $m = 1$, 2 and 3, respectively. The different system sizes correspond to different colors as indicated in the legend.

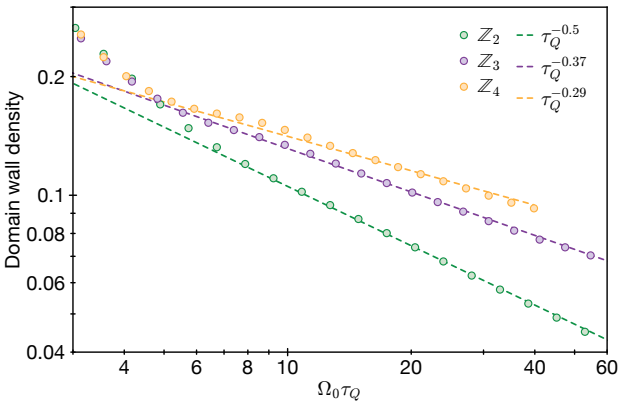

Figure S11: **Kibble-Zurek scaling in the m-site blockade model.** The system is initialized in the state $|0\rangle^{\otimes N}$, i.e., the ground state at $\Omega = 0$, $\Delta < 0$. Then, a quench is performed with profile $\Omega(t) = \Omega_0 \sin^2(\pi t/\tau_Q)$, and $\Delta(t) = 10\Omega_0(2t/\tau_Q - 1) + \Delta_c$, with Δ_c obtained by finite-size scaling in Fig. S10. We show the final defect density as a function of the quench time τ_Q for $m = 1$, $m = 2$ and $m = 3$, obtained via time-dependent MPS simulations with system sizes 54, 81 and 108 respectively. After a nonuniversal part for very short quenches, one can see a clear scaling behaviour with exponents consistent with those obtained from finite-size scaling (Fig. S10).

as

$$\tau = \begin{pmatrix} 1 & 0 & 0 \\ 0 & \omega & 0 \\ 0 & 0 & \omega^2 \end{pmatrix}, \quad \sigma = \begin{pmatrix} 0 & 1 & 0 \\ 0 & 0 & 1 \\ 1 & 0 & 0 \end{pmatrix}, \tag{19}$$

act locally on the site i, and each satisfy

$$\tau^3 = \sigma^3 = \mathbb{1}, \quad \sigma\,\tau = \omega\,\tau\,\sigma\,; \quad \omega \equiv \exp(2\,\pi\,\mathrm{i}/3)\,. \tag{20}$$

Here, ϕ and θ define two chiral interaction phases: for describing spatially ordered phases, we need $\phi = 0$, whereupon time-reversal and spatial-parity are both symmetries of the Hamiltonian but a purely spatial chirality is still present. Note that H_{Ryd} does not break time-reversal symmetry, necessitating the choice of $\phi = 0$ in the quantum clock model (18). However, with both ϕ and θ nonzero, time-reversal and spatial-parity (inversion) symmetries are individually broken, but their product is preserved.

As depicted in Fig. 4a, a generic state in the Hilbert space of the $\mathbb{Z}_3$ CCM can be mapped to one of three states of a clock according to the eigenvalue $1, \omega$, or ω^2 of the operator σ at each site. Consequently, there can be two domain walls in the system that differ in their energies, depending upon whether the clock rotates clockwise or counterclockwise upon crossing the wall. With $\phi = 0$

and $\theta \neq 0$, these have different energies, $2J\sin(\pi/6-\theta)$ and $2J\sin(\pi/6+\theta)$, and are thus inequivalent, leading to a chirality in the system that is absent for $\phi = \theta = 0$.

On setting both $\phi = \theta = 0$, $H_{\rm CCM}$ reduces to the Hamiltonian for the three-state Potts model which possesses a larger symmetry, $\mathbb{S}_3$; the concomitant order–disorder phase transition has critical exponents $z = 1$, $\nu = 5/6$ [64–66], and accordingly $\mu \approx 0.45$. Note that these exponents are fundamentally distinct from those of the $\mathbb{Z}_3$ CCM, namely, $z \approx 1.33$, $\nu \approx 0.71$, yielding $\mu \approx 0.37$. The Rydberg Hamiltonian described in the main text contains a point along the phase boundary for which the condition of $\phi = \theta = 0$ is fulfilled, and with fine tuned pulses it may be possible to explore the critical properties of the three-state Potts model.

For $n = 4$, the transitions of both the Potts and the achiral clock model are in the Ashkin-Teller universality class [67, 68]. The critical exponents of the four-state Potts model are $z = 1$, $\nu = 2/3$ (implying $\mu = 0.40$), whereas the four-state *achiral* clock model is equivalent to two uncoupled Ising systems with $z = 1$, $\nu = 1$. With a nonzero chirality, however, it is believed that there is no direct transition from the ordered to the disordered phase in the four-state CCM as an intermediate gapless incommensurate phase always intervenes [15, 31, 32].

[41] Endres, M. *et al.* Atom-by-atom assembly of defect-free one-dimensional cold atom arrays. *Science* **354**, 1024 (2016).

[42] Levine, H. *et al.* High-fidelity control and entanglement of Rydberg atom qubits. *arXiv:1806.04682* (2018).

[43] White, S. R. Density matrix formulation for quantum renormalization groups. *Phys. Rev. Lett.* **69**, 2863 (1992).

[44] White, S. R. Density-matrix algorithms for quantum renormalization groups. *Phys. Rev. B* **48**, 10345 (1993).

[45] Östlund, S. & Rommer, S. Thermodynamic limit of density matrix renormalization. *Phys. Rev. Lett.* **75**, 3537 (1995).

[46] Rommer, S. & Östlund, S. Class of ansatz wave functions for one-dimensional spin systems and their relation to the density matrix renormalization group. *Phys. Rev. B* **55**, 2164 (1997).

[47] Dukelsky, J., Martin-Delgado, M. A., Nishino, T. & Sierra, G. Equivalence of the variational matrix product method and the density matrix renormalization group applied to spin chains. *EPL* **43**, 457 (1998).

[48] Peschel, I., Wang, X., Kaulke, M. & Hallberg, K. (eds.)*Density-matrix Renormalization: A New Numerical Method in Physics.* Lecture Notes in Physics (Springer-Verlag, Berlin Heidelberg, 1999).

[49] McCulloch, I. P. Infinite size density matrix renormalization group, revisited. *arXiv:0804.2509v1* (2008).

[50] Pirvu, B., Murg, V., Cirac, J. I. & Verstraete, F. Matrix product operator representations. *New Journal of Physics* **12** (2010).

[51] Schollwöck, U. The density-matrix renormalization group. *Rev. Mod. Phys* **77**, 259 (2005).

[52] Schollwöck, U. The density-matrix renormalization group: a short introduction. *Phil. Trans. R. Soc. A* **369**, 2643 (2011).

[53] Whitsitt, S., Samajdar, R. & Sajdev, S. Quantum field theory for the chiral clock transition in one spatial dimension. *arXiv:1808.07056* (2018).

[54] Chepiga, N. & Mila, F. Floating phase versus chiral transition in a 1D hard-boson model. *arXiv:1808.08990* (2018).

[55] Gerster, M., Haggenmiller, B., Tschirsich, F., Silvi, P. & Montangero, S. Dynamical Ginzburg criterion for the quantum-classical crossover of the Kibble-Zurek mechanism. *arXiv:1807.10611* (2018).

[56] Moessner, R., Sondhi, S. L. & Fradkin, E. Short-ranged resonating valence bond physics, quantum dimer models, and Ising gauge theories. *Phys, Rev. B* **65**, 024504 (2001).

[57] Fisher, M. E. & Barber, M. N. Scaling theory for finite-size effects in the critical region. *Phys. Rev. Lett.* **28**, 1516 (1972).

[58] Hamer, C. J. & Barber, M. N. Finite-size scaling in Hamiltonian field theory. *J. Phys. A: Math. Gen.* **13**, L169 (1980).

[59] Huse, D. A. Simple three-state model with infinitely many phases. *Phys. Rev. B* **24**, 5180 (1981).

[60] Huse, D. A., Szpilka, A. M. & Fisher, M. E. Melting and wetting transitions in the three-state chiral clock model. *Physica A* **121**, 363 (1983).

[61] Fendley, P. Parafermionic edge zero modes in $\mathbb{Z}_n$-invariant spin chains. *J. Stat. Mech* **11**, 11020 (2012).

[62] Zhuang, Y., Changlani, H. J., Tubman, N. M. & Hughes, T. L. Phase diagram of the Z3 parafermionic chain with chiral interactions. *Phys. Rev. B* **92**, 035154 (2015).

[63] Sachdev, S., Sengupta, K. & Girvin, S. M. Mott insulators in strong electric fields. *Phys. Rev. B* **66**, 075128 (2002).

[64] Wu, F.-Y. The Potts model. *Rev. Mod. Phys.* **54**, 235 (1982).

[65] Alexander, S. Lattice gas transition of He on Grafoil. A continous transition with cubic terms. *Phys. Lett. A* **54**, 353 (1975).

[66] Baxter, R. J. Hard hexagons: exact solution. *J. Phys. A: Math. Gen* **13**, L61 (1980).

[67] José, J. V., Kadanoff, L. P., Kirkpatrick, S. & Nelson, D. R. Renormalization vortices, and symmetry-breaking perturbations in the two-dimensional planar model. *Phys. Rev. B* **16**, 1217 (1977).

[68] Kadanoff, L. P. Connections between the critical behavior of the planar model and that of the eight-vertex model. *Phys. Rev. Lett.* **39**, 903 (1977).